Determining conditions that allow a shear margin to coincide with a Röthlisberger channel

John D. Platt[1,2], Thibaut Perol,[1], Jenny Suckale[3], and James R. Rice[1,4]

[1]Harvard John A. Paulson School of Engineering and Applied Sciences, Harvard University, Cambridge, Massachusetts, USA.

[2]Now at, Department of Terrestrial Magnetism, Carnegie Institution for Science, Washington DC, USA.

[3]Department of Geophysics, Stanford University, Palo Alto, California, USA.

[4]Department of Earth and Planetary Sciences, Harvard University, Cambridge, Massachusetts, USA.

This article has been accepted for publication and undergone full peer review but has not been through the copyediting, typesetting, pagination and proofreading process, which may lead to differences between this version and the Version of Record. Please cite this article as doi: 10.1002/2015JF003707

Abstract.

The mass loss from the West Antarctic Ice Sheet is dominated by numerous rapidly flowing ice streams, which are separated from stagnant ice in the adjacent ridges by zones of concentrated deformation known as shear margins. Because the discharge from a single ice stream depends sensitively on the ice stream width, determining the physical processes that control shear margin location is crucial to a full understanding of ice stream dynamics. Previous work has shown that the transition from a deforming to an undeforming bed within a shear margin concentrates large stresses on the undeforming bed beneath the ridge [*Jacobson and Raymond*, 1998; *Schoof*, 2004; *Suckale et al.*, 2014]. In this paper we investigate how the presence of a drainage channel collocated with the transition from a deforming to an undeforming bed perturbs the stress field within the shear margin. We show that the channel limits the maximum shear stress on the undeforming bed and alters the yield strength of the till by changing the normal stress on the ice-till interface. By comparing the maximum stress with the till strength, we show that the transition from a deforming to an undeforming bed can occur across a channel whenever the water flux in the channel exceeds a critical value. This critical flux is sensitive to the rheology and loading of the shear margin, but we conclude that there are some scenarios where the transition from a deforming to an undeforming bed can be collocated with a drainage channel, though this configuration is probably not typical.

1. Introduction

Surface velocity observations of the West Antarctic Ice Sheet show that ice flow is highly non-uniform, with regions of $\sim 20-80$ km width known as ice streams flowing much faster than the surrounding ice sheet. Despite accounting for a fraction of the surface area of the ice sheet, rapidly flowing ice streams dominate the discharge of ice from the continent [*Bamber et al.*, 2000]. Thus, determining the physical processes that govern ice stream dynamics is of the utmost importance to understanding how West Antarctica will respond to a changing climate.

Typically ice streams have an ice thickness of one kilometer, a width of a few tens of kilometers, and a length of a few hundred kilometers. The surface velocity in the center of an ice stream is a few hundreds of meters per year, which is significantly larger than the surface velocity of a few meters per year in the surrounding ice sheet. Rapid flow is possible despite the low gravitational stress driving deformation ($\sim$ 10 kPa) because of the presence of a saturated subglacial till layer beneath the ice stream [*Blankenship et al.*, 1986, 1987]. The pore pressure in the till layer is close to the ice overburden, leading to a low effective stress. For the Coulomb-plastic rheology typically observed in laboratory experiments on subglacial till [*Kamb*, 1991; *Iverson et al.*, 1998; *Tulaczyk et al.*, 2000], a low effective stress produces a low yield strength. Thus, the subglacial till provides limited resistance to flow and a substantial fraction of the ice stream surface velocity is accommodated by till deformation [*Alley et al.*, 1986].

A zone of concentrated deformation known as a shear margin separates the rapidly flowing ice stream from the stagnant ice in the adjacent ridge. Shear margins are typ-

ically a few kilometers wide and marked by extensive surface crevassing [*Bindschadler and Vornberger*, 1990; *Echelmeyer et al.*, 1994; *Scambos et al.*, 1994]. Because the till provides limited resistance to motion, shear margins balance a substantial fraction of the gravitational driving stress [*Echelmeyer et al.*, 1994; *Jackson and Kamb*, 1997; *Harrison et al.*, 1998; *Joughin et al.*, 2002]. The shear margin location also sets the width of the ice stream, and thus plays an important role in determining the ice stream discharge [*van der Veen and Whillans*, 1996; *Raymond*, 1996; *Raymond et al.*, 2001]. Despite the important role shear margins play in ice stream dynamics, the physical processes that select their location are still uncertain. In contrast with mountain glaciers, topography alone does not appear to explain current shear margin locations of Siple Coast ice streams [*Shabtaie and Bentley*, 1987, 1988; *Raymond et al.*, 2001], and thus shear margin location in this case must depend on the mechanical properties of ice and till.

Within a shear margin, there must be a transition from a deforming bed beneath an ice stream, where the stress on the bed reaches the yield strength of the subglacial till and plastic deformation occurs, to an undeforming bed beneath the ridge, where the stress is always less than the yield strength of the till. Henceforth we refer to the point where this transition occurs as the locking point. For ice streams where the shear margins support a substantial fraction of the gravitational driving stress the mechanical transition at the locking point concentrates stress on the undeforming bed, so for a shear margin to exist there must be a mechanism that raises the yield strength of the undeforming bed far above the yield strength inferred beneath the majority of the ice stream. One strengthening mechanism that is commonly appealed to is freezing of the subglacial till, as studied by *Jacobson and Raymond* [1998], *Schoof* [2012], and *Haseloff* [2015]. Alternatively, *Perol et*

al. [2015] proposed that melt generated by concentrated deformation in the shear margins feeds a subglacial drainage channel at the base of the shear margin. This drainage channel allows more efficient drainage than the distributed hydrologic system that operates under the remainder of the ice stream, and decreases the pore pressure in a zone of kilometer-scale width within the shear margin. For a Coulomb-plastic rheology, reducing the pore pressure raises the yield strength of the till, allowing a stable margin configuration to form if the locking point is not collocated with the channel. Here we define a stable margin configuration to be one for which the shear stress resolved on the bed is less than the yield strength of the till wherever the bed is undeforming. We use the term stable to describe such a configuration because if the stress exceeds the strength anywhere on the undeforming bed then that portion of the bed will yield and the ice stream will widen.

In this paper we investigate under what conditions the locking point can be collocated with a drainage channel. This analysis complements *Perol et al.* [2015], which investigated how a drainage channel not collocated with the locking point can select the margin location. The crucial consideration in this manuscript is how the presence of a channel alters the stress field around the locking point, while *Perol et al.* [2015] primarily focused on how the channel raises the yield strength of the till over a broad zone within the shear margin. To begin we show that a sharp transition (i.e. no drainage channel) generally leads to a singular stress profile on the undeforming bed, an obviously unphysical scenario because the yield strength of the undeforming bed is finite. Next we show that the presence of a channel at the locking point limits the maximum shear stress on the undeforming bed and alters the yield strength of the till by changing the normal stress on the ice-till interface. Comparing the maximum stress on the undeforming bed with the till strength

we investigate when the locking point can be collocated with a channel. Our results lead to a critical water flux in the channel that must be exceeded for the transition from a deforming to an undeforming bed to occur across a channel. For a Glen's law rheology this critical flux is unrealistically large if the average lateral shear stress in the shear margin exceeds $\sim 35 - 50$ kPa. However, for the dislocation creep rheology of *Durham et al.* [1997], which is governed by a stress exponent of four, that dominates near the transition from a deforming to an undeforming bed if grain sizes are greater than a few millimeters (for smaller grain sizes deformation falls into the grain boundary sliding regime explored in *Goldsby and Kohlstedt* [2001]) the critical flux is substantially lower, and the locking point can be collocated with the channel if the average lateral shear stress in the shear margin is less than $\sim 85-115$ kPa. Using data for a range of shear margins from *Joughin et al.* [2002], *Perol and Rice* [2015] estimated that $\tau_{lat} \approx 100-135$ kPa. Thus, we conclude that there are some scenarios where the locking point can be collocated with a drainage channel, though this configuration is probably not typical.

Though this manuscript revolves around a subglacial drainage channel, one of the key elements in many subglacial hydrology models, our focus is not on modeling how large scale variations in subglacial hydrology influence ice stream dynamics. Instead, we focus on how the presence of a drainage channel alters the stress field at the base of a shear margin on length scales of a few tens of meters. These length scales are small enough that spatial variations in pore pressure are negligible if we assume typical permeabilities for subglacial till. Our results show that the transition from a deforming to an undeforming bed within a shear margin can occur across a channel if the water flux in the channel exceeds a critical value, providing a natural path to incorporating our work into larger

scale models of subglacial hydrology. Our work complements several recent papers that focus on how large scale variations in subglacial hydrology influence ice sheet dynamics on a range of time and length scales. Most closely related to our work, *Perol et al.* [2015] showed that the presence of drainage channel can select the location of the locking point by raising the yield strength of the till over a broad zone within the shear margin. On a larger scale, *Kyrke-Smith et al.* [2014] and *Kyrke-Smith et al.* [2015] investigated how the coupling between ice flow and subglacial hydrology controls the formation and spacing of ice streams. Finally, on a much shorter timescale, *Schoof* [2010] showed how variations in surface melt influence ice velocity by driving rapid changes in the efficiency of subglacial drainage.

2. Model derivation

Here we develop a model for ice deformation near the locking point. We define the coordinate vector $\mathbf{x} = (x, y, z)$ so that x is parallel to the direction of ice stream flow, y is parallel to the bed and perpendicular to the ice stream margin, and z is the vertical height above the bed (see Figure 1). The transition from a deforming to an undeforming bed occurs across a semi-circular drainage channel centered on $y = z = 0$, with the ice stream located in $y < 0$ and the ridge located in $y > 0$. We define the velocity vector $\mathbf{u} = (u, v, w)$ such that u is the velocity in the x-direction, v the velocity in the y-direction, and w the velocity in the z-direction.

As is common when modeling flow in ice stream margins [*Jacobson and Raymond*, 1998; *Schoof*, 2004, 2012; *Suckale et al.*, 2014; *Perol et al.*, 2015], we assume that all flow is in the downstream direction, making u the only non-zero component in the velocity vector, and that u is independent of x. These assumptions are justified by surface velocity

observations of ice streams showing that the downstream velocity is much greater than the lateral and vertical velocities v and w and that variations in u in the downstream direction are much smaller than variations in the lateral and vertical directions. The single non-zero component of the velocity vector $u(y, z)$ leads to just two non-zero shear strain rates,

$$\dot{\varepsilon}_{xy} = \frac{1}{2}\frac{\partial u}{\partial y} \quad , \quad \dot{\varepsilon}_{xz} = \frac{1}{2}\frac{\partial u}{\partial z}. \tag{1}$$

These lead to two non-zero shear stresses τ_{xy} and τ_{xz}, and the equations for mechanical equilibrium simplify to

$$\frac{\partial \tau_{xy}}{\partial y} + \frac{\partial \tau_{xz}}{\partial z} = 0, \tag{2}$$

describing a stress/deformation state called "anti-plane". In the next section we show that the transition from a deforming to an undeforming bed concentrates large stresses at the locking point, with typical shear stresses of a few hundred kPa. Since these shear stresses are much greater than the gravitational driving stress for the ice stream, which is typically ~ 10 kPa, we can neglect the driving stress when solving for the stress field at the locking point using equation (2). However, as shown in Section 3, the gravitational driving stress still enters into our model by providing the far-field loading on the locking point, which is parameterized using a path-independent integral.

To close the model we need a rheological law linking strain rate and shear stress. Though ice can deform through a variety of mechanisms linked to physical phenomena such as dislocation motion and diffusion [*Schulson and Duval*, 2009], we assume a single deformation mechanism with a power law dependence,

$$\epsilon_{ij} = A\tau_E^{n-1}\tau_{ij}, \tag{3}$$

where $\tau_E = [\tau_{xy}^2 + \tau_{xz}^2]^{1/2}$ is the effective shear stress and $\epsilon_E = [\epsilon_{xy}^2 + \epsilon_{xz}^2]^{1/2}$ is the effective strain rate. Since the channel is expected to lie within the temperate ice zone [*Suckale et al.*, 2014; *Perol and Rice*, 2015], we assume for the local analysis of stressing near the channel that temperature, and hence A and n, are spatially uniform. In addition we neglect any dependence of A and n on melt fraction in the temperate ice, which may be a poor assumption for a channel with a well-developed englacial drainage system.

Equation (3) can model different deformation mechanisms by assuming different values of A and n. The majority of calculations in this paper assume a Glen's law rheology with $n = 3$ and $A = 2.4 \times 10^{-24}$ Pa^{-3} s^{-1}, which are the values recommended in *Cuffey and Paterson* [2010] for $T = 0$ °C. However, *Goldsby and Kohlstedt* [2001] showed that Glen's original data plots on the boundary between two deformation mechanisms with stress exponents of 1.8 and 4, which may explain why Glen best fit his data with n = 3 (see Figure 60.3 of *Goldsby* [2006].) Thus, we also model the dislocation creep rheology of *Durham et al.* [1997] using $n = 4$ and $A = 2.2 \times 10^{-30}$ Pa^{-4} s^{-1}, which may dominate at the large shear stresses attained in the shear margin depending on exact values of temperature and grain size [*Goldsby*, 2006]. Finally, we produce some results using a Newtonian rheology with $n = 1$ and $A = 2.4 \times 10^{-14}$ Pa^{-1} s^{-1}, where this value of A the effective viscosity predicted by Glen's law evaluated at 100 kPa (a typical shear stress in a shear margin).

3. Deformation around a sharp transition

As noted in *Suckale et al.* [2014], the deformation near the locking point is equivalent to an anti-plane shear crack in a creeping solid. Recognizing this correspondence, we use

methods from fracture mechanics to solve for the stress and velocity fields around a sharp transition from a deforming to an undeforming bed at $y = 0$.

Following *Rice* [1967] and *Rice* [1968b], Appendix A develops a solution for the stress field and velocity field around a sharp transition from a deforming to an undeforming bed. Note that the solution for the stress around a sharp transition was previously developed in *Suckale et al.* [2014] and used to benchmark numerical solutions for velocity and heat production in a shear margin, but the physical significance of the singular stress field and the implications for the mechanical structure of a shear margin were not emphasized. The shear stress component τ_{xz} on the undeforming bed ($z = 0$ and $y > 0$) is given by

$$\tau_{sharp} = \left(\frac{n J_{tip}}{(n+1) A \pi y} \right)^{1/(n+1)} . \tag{4}$$

The far-field loading is linked to the stress at the locking point using the path-independent integral from *Suckale et al.* [2014], leading to

$$J_{tip} = \frac{4 H A \tau_{lat}^{n+1}}{n+1} \quad , \quad \tau_{lat} = \left(\rho_{ice} g S - \frac{\tau_{base}}{H} \right) \frac{W}{2}. \tag{5}$$

Here H is the ice thickness, W is the ice stream width, ρ_{ice} is the ice density, g is gravity, $S > 0$ is the slope in the downstream direction, and τ_{base} is the basal resistance provided by the deforming bed. A simple force balance for the ice stream shows that τ_{lat} is the average lateral drag supported by the shear margin. The path-independent integral in *Suckale et al.* [2014] is an extension of the J-type integrals first introduced for cracks in elastic solids by *Rice* [1968a], *Cherepanov* [1968] and *Bilby and Eshelby* [1968], later generalized to the nonlinear creep rheologies we consider (e.g. *Goldman and Hutchinson* [1975], *Landes and Begley* [1976], *Kubo et al.* [1979], *Ben Amar and Rice* [2002]), and previously applied to glaciers by *McMeeking and Johnson* [1986]. Inserting equation (5)

into equation (4) we find

$$\tau_{sharp} = \tau_{lat} \left(\frac{4Hn}{(n+1)^2 \pi y} \right)^{1/(n+1)} . \quad (6)$$

The lateral stress supported by the shear margin is transmitted to the undeforming bed beneath the ridge such that the stress on the undeforming bed is directly proportional to the lateral drag supported by the shear margin. Note that equation (5) is only valid when the J-integral is evaluated using a constant basal resistance beneath the ice stream, though the solution can be easily extended to account for a spatially variable basal resistance.

Equation (6) has three distinctive features. First, the shear stress on the undeforming bed is singular with infinite shear stresses on the undeforming bed expected at the locking point. Second, the power of the singularity depends on the stress exponent n, with larger values of n corresponding to less severe singularities. Finally, larger values of τ_{lat} concentrate larger stresses on the undeforming bed. A singular stress field is obviously unphysical due to the finite yield strength of the bed. *Schoof* [2004] and *Perol et al.* [2015] avoided this problem by using a spatially variable shear strength profile at the bed to find non-singular solutions where the stress concentration vanishes. This is equivalent to solving for the transition from a deforming to an undeforming bed that satisfies $J_{tip} = 0$, which produces a continuous stress at the locking point. The solutions of *Schoof* [2004] and *Perol et al.* [2015] are analogous to the cohesive zone models commonly used in fracture mechanics to eliminate crack tip singularities by appealing to a zone of enhanced resistance near the crack tip [*Barenblatt*, 1959; *Dugdale*, 1960; *Bilby et al.*, 1963]. We take a different approach where J_{tip} is finite but the maximum stress on the bed is limited by the presence of a channel at the locking point. Our approach is analogous to crack blunting in fracture mechanics, which relies on the maximum stress at the crack tip decreasing as

the radius of curvature of the crack (or now notch) tip increases. Note that our crack blunting mechanism for a finite value of J_{tip} is only valid if the locking point coincides with a channel (if not the shear stress on the bed is singular for non-zero values of J_{tip}). However, even if the locking point is not collocated with a channel, the presence of a drainage channel can still select the location of the locking point by raising the yield strength of the till over a broad zone within the shear margin, as shown in *Perol et al.* [2015] who model the hydrology of transport and pore fluid suction development along the interface.

To begin we show that all the information about the far-field loading is transmitted to the locking point through J_{tip} alone. To do this we compare the analytic prediction valid near the locking point (see Appendix A) with results from numerical simulations generated using the finite element package COMSOL for the whole ice stream model that couples temperature and deformation from *Perol et al.* [2015]. Since the analytic solution has a fixed functional form with a single free parameter J_{tip} we should be able to match the numerical solutions over a range of r and θ using a single value of J_{tip}. Figure 2 shows the match between the analytic and numerical solutions by plotting the downstream velocity as a function of θ at five different values of r, as well as the shear stress on the undeforming bed. The specific value of J_{tip} used to plot the analytic solution is found by fitting to the numerical solution for downstream velocity at $r = 5$ m and this value is used to plot the downstream velocity profile at other values of r as well as the stress on the undeforming bed. In Figure 2 one simulation is performed for a temperature independent rheology and a second simulation for the full temperature dependent rheology given in *Perol et al.* [2015]. Since the two solutions are in good agreement for all curves plotted in Figure 2,

our results demonstrate that the asymptotic solution presented in Appendix A provides a good approximation to the full numerical solution for several tens of meters around the locking point.

We can exploit the fact that the length scale over which the analytic and numerical solutions agree is at least an order of magnitude greater than the estimates for channel radius in *Perol et al.* [2015] by making an approximation analogous to the small-scale yielding approximation commonly used in fracture mechanics when the process zone at the crack tip is small enough that the entire body can be treated as an elastic solid in a continuum model [*Rice*, 1967, 1968b]. The equivalent approximation in our model is that the region over which the channel perturbs the stress field is contained entirely within the zone of validity for the asymptotic solution at a sharp transition from a deforming to an undeforming bed, and thus all knowledge of the far-field deformation is transmitted to the channel through the asymptotic solution. Even though the entire ice is creeping in our model, henceforth we follow the terminology used in fracture mechanics and refer to our approach as making a small-scale yielding approximation. The small-scale yielding approximation allows us to draw two important conclusions. First, it tells us that all information about the far-field deformation is carried to the locking point through a single parameter J_{tip}, which controls the magnitude of the stresses in the asymptotic solution valid at the transition from a deforming to an undeforming bed. Thus, ice stream scale parameters such as W and τ_{base} influence the stress at the locking point only through J_{tip}, greatly reducing the number of independent parameters we must consider. Second, the small-scale yielding approximation allows us to study the spatial variations in stress

around a channel at the locking point by imposing the asymptotic solution from Appendix A as a boundary condition far from the channel.

4. Stress field around a channel

Next, we investigate how a channel with a radius R at the locking point alters the shear stress resolved on the undeforming bed. Since we neglect to model the stress field within the till and only solve for the stress field within the ice, the exact point within the channel where the bed transitions from deforming to undeforming is unimportant. All that matters is that the bed on one side of the channel is deforming and the bed on the other side is undeforming. Within the channel the shear stress on the till is controlled by turbulent flow of water, which is unlikely to be large enough to cause the till to yield for typical effective pressures in the channel but may allow erosion of the till to occur. A sketch of the geometry assumed in our calculation can be found in Figure 1. To begin, we use a complex variable method to solve analytically for a Newtonian rheology, then use numerical simulations to extend our analysis to a power law rheology.

As discussed in Section 3, from our analogy with fracture mechanics we expect the presence of a channel to limit the maximum stress on the undeforming bed to a finite value that decreases as the channel radius increases. Our goal in this section is to quantify how the stress on the undeforming bed varies with parameters such as channel radius, ice stream width, and the average basal resistance beneath the ice stream. The small-scale yielding approximation justified in the previous section greatly reduces the number of independent parameters that influence the stress on the undeforming bed. Ice stream scale parameters such as W and τ_{base} influence the stress at the locking point only through J_{tip}. The significant reduction in the number of independent parameters allows us to

use dimensional analysis to tightly constrain the functional form of the stress on the undeforming bed. We find that the stress on the bed is a function of J_{tip}/A, R, n, and y alone. There is a single way to combine these parameters to produce a quantity with units of stress, and thus the stress on the undeforming bed is equal to

$$\tau = \tau_{sharp}(R) h\left(\frac{y}{R}, n\right), \tag{7}$$

where τ_{sharp} is the singular solution for a sharp transition given in equation (4) and h is a function we must solve for. For all cases the maximum stress on the bed, which is where the undeforming bed is most likely to yield, occurs at the channel wall and is equal to

$$\tau_{max} = \chi \tau_{sharp}(R), \tag{8}$$

where $\chi = h(1, n)$ is a function of the stress exponent n alone. Thus, if we can determine how the parameter χ depends on the stress exponent n then equation (8) provides a completely general solution that allows us to predict the maximum shear stress on the undeforming bed for any set of parameter choices.

4.1. Newtonian rheology

For a Newtonian rheology we can make significant progress analytically. When $n = 1$ the equation for mechanical equilibrium reduces to Laplace's equation,

$$\frac{\partial^2 u}{\partial r^2} + \frac{1}{r}\frac{\partial u}{\partial r} + \frac{1}{r^2}\frac{\partial^2 u}{\partial \theta^2} = 0, \tag{9}$$

where r and θ are polar coordinates centered on the origin. We solve equation (9) in $R < r < \infty$ with the no slip boundary condition on the undeforming bed,

$$u = 0 \quad \text{on} \quad \theta = 0,\ R < r < \infty, \tag{10}$$

and the traction free boundary condition on the deforming bed,

$$\frac{\partial u}{\partial \theta} = 0 \quad \text{on} \quad \theta = \pi,\ R < r < \infty. \tag{11}$$

An additional traction free boundary condition is applied on the channel wall,

$$\frac{\partial u}{\partial r} = 0 \quad \text{on} \quad r = R,\ 0 < \theta < \pi. \tag{12}$$

Finally we assume that u approaches the solution for a sharp transition developed in appendix A as $r \to \infty$, consistent with our small-scale yielding approximation.

Equations (9)-(12) are solved using complex variables in Appendix B, leading to the shear stress on the undeforming bed,

$$\tau_{xz} = \left(\frac{J_{tip}}{2A\pi y}\right)^{1/2} \left(1 + \frac{R}{y}\right). \tag{13}$$

We notice two distinctive features about this solution. First, the solution for a sharp transition is the asymptotic limit of equation (4) when $y \gg R$. Thus, the presence of a channel only alters the stress field on the bed in the immediate vicinity of the channel, and far from the channel the stress field is the same as that predicted for a sharp transition. Second, the presence of the channel caps the maximum shear stress on the bed at a finite value,

$$\tau_{max} = \left(\frac{2J_{tip}}{A\pi R}\right)^{1/2}. \tag{14}$$

Note that a larger channel radius R leads to a lower maximum shear stress on the bed. Comparing equation (14) to the solution for a sharp transition we find

$$\tau_{max} = 2\tau_{sharp}(R), \tag{15}$$

and thus $\chi = 2$ for $n = 1$. The maximum stress applied to the bed is equal to twice the stress predicted by evaluating the singular solution for a sharp transition at the channel

radius R. As highlighted before, the finite maximum stress allows for a stable margin configuration where the stress on the undeforming bed is always less than the yield strength of the bed even when $J_{tip} \neq 0$.

4.2. Nonlinear rheology

The complex variable solution presented in the previous subsection cannot be generalized to a nonlinear rheology so we study other values of the stress exponent n using numerical solutions. We use a finite difference method on a uniform gird in r and θ and enforce the far-field velocity field given by equation (A24) on a semi-circular boundary with radius D. The traction free boundary condition on the channel wall remains the same as in the previous subsection and the boundary conditions on the bed are now applied for $R < r < D$. The finite domain size introduces an additional dimensionless parameter R/D into equation (7), but we expect to recover the solution where the boundary conditions are applied at infinity as $R/D \to 0$.

The homogeneous boundary conditions allow us to calculate the dependence of χ on R/D analytically for $n = 1$. We find

$$\chi = 2\left(1 + \frac{R}{D}\right)^{-1}. \tag{16}$$

As expected, $\chi \to 2$ as $R/D \to 0$. Next we determine how χ depends on R/D for several values of n numerically. Figure 3 shows how χ varies with R/D for $n = 1$, $n = 3$, and $n = 4$ when the channel radius is fixed at $R = 1$ m and the outer radius D is varied. To perform these simulations we assume an ice thickness of 1 km, an ice stream width of 34 km, a slope $S = 0.0012$, and a basal stress of $\tau_{base} = 3.5$ kPa. These parameters are intended to model Dragon margin of Ice Stream B2 and are equivalent to $\tau_{lat} = 124$ kPa.

We observe a weak dependence of χ on R/D for all n, with larger values of R/D leading to smaller values of χ. Our analytic solution for $n = 1$ allows us to guess a functional form for this dependence,

$$\chi = \chi_{inf}(n) \left(1 + \frac{R}{D}\right)^{-\frac{1}{n}}, \tag{17}$$

which is shown by dashed curves in Figure 3. We infer best fitting values for χ_{inf} of 1.15 for $n = 3$ and 1.09 for $n = 4$. The final form for the maximum stress on the bed is

$$\tau_{max} = \chi(n) \left(\frac{nJ_{tip}}{(n+1)A\pi R}\right)^{1/(n+1)}. \tag{18}$$

where $\chi(n)$ is set to the value inferred in Figure 3 as $R/D \to 0$ (i.e. χ_{inf}).

Numerical simulations also allow us to study the spatial variations in shear stress on the undeforming bed when a channel is present. Figure 4 shows the stress on the undeforming bed for $n = 1$ and $n = 3$ and the parameters in Table 1. As the stress exponent increases the maximum stress on the undeforming bed drops significantly, in excellent agreement with the behavior predicted for a sharp transition in equation (4) that showed a strong dependence of the singularity on the stress exponent. Our simulations show that for $n = 3$ and $n = 4$ the stresses calculated numerically accounting for the channel are comparable to the predictions for a sharp transition for several tens of meters adjacent to the channel.

4.3. The importance of basal resistance

Up until now we have neglected the basal resistance beneath the ice stream when solving for the stress field around the locking point, arguing that τ_{base} is much smaller than the large stresses concentrated near the locking point. While this is true for values of the basal resistance inferred beneath the majority of an ice stream – typically $1 - 5$ kPa [*Kamb*, 2001] – it may not be true for the large basal resistance we expect to occur near a channel

[*Perol et al.*, 2015]. We can make some simple estimates analytically if we assume that $n = 1$ and the basal resistance immediately adjacent to the channel takes a uniform value τ_f, which is linked to but potentially much greater than τ_{base}. As shown in Appendix B, the stress on the undeforming bed is

$$\tau_{xz} = \tau_f + \sqrt{\frac{J_{tip}}{2\pi A y}} \left(1 + \sum_{n=1}^{\infty} C_n \left(\frac{R}{y} \right)^n \right), \tag{19}$$

where the constants C_n are given in equations (B18) and (B19). Figure 5 plots the stress on the undeforming bed for different values of τ_f using the parameters in Tables 1 and 2. Our results show that for these parameter choices the dependence of maximum stress on τ_f is not significant, with the maximum stress on the bed increasing by approximately 25% as τ_f varies by 600 kPa. To explore the dependence on τ_f for other parameter choices we use equation (19) to calculate the maximum stress on the bed,

$$\tau_{max} = \left(1 + \frac{4}{\pi} \right) \tau_f + \sqrt{\frac{2 J_{tip}}{\pi A R}}. \tag{20}$$

Comparing the magnitude of the two terms in equation (20) we conclude that for all values of J_{tip} the maximum stress resolved on the bed increases with τ_f, and this increase can be significant if τ_f is comparable to $\tau_{sharp}(R)$. Note that even when $J_{tip} = 0$ the maximum shear stress on the undeforming bed exceeds the yield strength of the deforming bed.

Our analysis could be extended to account for a nonlinear rheology and a spatially variable basal resistance on the deforming bed numerically. However, as discussed in more detail in Section 7.1, the exact form of the spatial variations in basal resistance is currently unclear, and is complicated by many additional processes not accounted for here including the coupling between in-plane and anti-plane deformation, a change in boundary conditions across the channel, and changes in channel geometry due to asymmetric creep

closure. If our conclusion that the importance of τ_f increases as τ_f approaches $\tau_{sharp}(R)$ holds for $n \neq 1$ then we expect basal resistance to become more important as the stress exponent increases because the maximum stress on the bed decreases with increasing n.

5. Basal yield strength adjacent to channel

Here we model the yield strength of the undeforming bed adjacent to the channel, which is governed by a Coulomb-plastic rheology controlled by the effective stress in the till and a friction coefficient

$$\tau_{yield} = f(\sigma_n - p), \tag{21}$$

where σ_n is the normal stress acting on the bed, p is the pore pressure, and f is the friction coefficient of the till.

To determine the effective stress of the bed we model a steady state channel following the approach from *Röthlisberger* [1972]. First, we use the Gauckler-Manning law for turbulent flow in a conduit to relate the water flux in the channel Q_w to the channel geometry through

$$\frac{Q_w}{A_{ch}} = \frac{R_h^{2/3} S^{1/2}}{n_m}, \tag{22}$$

where A_{ch} is the area of the channel, R_h is the hydraulic radius of the channel, and n_m is the Gauckler-Manning coefficient. For the semi-circular channel shown in Figure 1,

$$A_{ch} = \frac{\pi R^2}{2} \quad , \quad R_h = \frac{R}{2(1 + 2/\pi)}. \tag{23}$$

Combining equations (22) and (23) we solve for the channel radius,

$$R = 2^{5/8} \left(\frac{n_m Q_w}{\pi S^{1/2}} \right)^{3/8} \left(1 + \frac{2}{\pi} \right)^{1/4}. \tag{24}$$

Note that for fixed values of n_m and S the channel radius is a function of the water flux alone, with larger water fluxes leading to a larger channel radius.

The heat generated by turbulent flow in the channel leads to melting at the channel wall [*Röthlisberger*, 1972; *Shreve*, 1972]. Using the rate at which water flowing in the channel converts gravitational potential energy into heat we calculate the rate at which melting expands the channel radius,

$$\dot{R}_{melt} = \frac{\rho_w g S Q_w}{\pi L \rho_{ice} R}, \tag{25}$$

where ρ_w is the density of water and L is the latent heat of fusion for ice. Melting at the channel interface is balanced by creep closure of the channel due to the ice overburden. For the power law rheology given in equation (3) we use the solution from *Nye* [1953] for creep closure of a circular channel to estimate the closure rate as,

$$\dot{R}_{creep} = \frac{AR\left(\sigma_o - p\right)^n}{n^n}, \tag{26}$$

where $\sigma_o = \rho_{ice} g H$ is the ice overburden pressure. A steady state size occurs when melting at the channel wall exactly balances creep closure. Setting (25) equal to (26) we find that the pore pressure in the channel is equal to

$$p = \sigma_o - n\left(\frac{\rho_w g S Q_w}{\pi A L \rho_{ice} R^2}\right)^{1/n}. \tag{27}$$

Note that the pore pressure decreases as the flux within the channel increases, and thus the till yield strength in the vicinity of the channel increases with Q_w.

Perol et al. [2015] showed that hydraulic diffusion equilibrates the pore pressure in the till with the pore pressure in the channel over the few tens of meters immediately adjacent to the channel. However, the presence of a channel alters the yield strength immediately adjacent to the channel by changing the normal stress resolved on the till. We can use

the creep closure solution from *Nye* [1953] to determine the normal stress resolved on the till adjacent to the channel,

$$\sigma_n = p + (\sigma_o - p)\left(1 + \frac{2-n}{n}\left(\frac{R}{y}\right)^{2/n}\right). \tag{28}$$

Combining equations (27) and (28) with the Coulomb-plastic rheology from equation (21) we calculate the strength of undeforming bed to be

$$\tau_{yield} = f\left(\frac{\rho_w g S Q_w}{\pi A L \rho_{ice} R^2}\right)^{1/n}\left(n + (2-n)\left(\frac{R}{y}\right)^{2/n}\right). \tag{29}$$

Equation (29) predicts large changes in the yield strength of the undeforming bed in the immediate vicinity of the channel, with the strength increasing near the channel for $n < 2$ but decreasing near the channel for $n > 2$. The yield strength at the channel wall, where the highest shear stress is resolved on the bed, is

$$\tau_{yield} = 2f\left(\frac{\rho_w g S Q_w}{\pi A L \rho_{ice} R^2}\right)^{1/n}. \tag{30}$$

6. Stable margin configurations

To determine when the locking point can be stably collocated with a channel we compare the maximum stress on the undeforming bed with the yield strength at the channel wall. We focus on a Glen's law rheology but generalize our analysis to other stress exponents in Appendix C. Assuming that the bed first yields at the channel wall, where the maximum shear stress on the bed is greatest, we use equations (18) and (30) to write the condition for a stable margin configuration as

$$\chi\left(\frac{3J_{tip}}{4\pi A R}\right)^{1/4} < 2f\left(\frac{\rho_w g S Q_w}{\pi A L \rho_{ice} R^2}\right)^{1/3}. \tag{31}$$

We rearrange the inequality to find that a stable margin configuration only occurs when the channel radius is less than the critical locking radius

$$R_{lock} = \left(\frac{2f}{\chi}\right)^{12/5} \left(\frac{\rho_w g S Q_w}{\pi A L \rho_{ice}}\right)^{4/5} \left(\frac{4\pi A}{3J_{tip}}\right)^{3/5}. \quad (32)$$

Even though larger channels are more effective at limiting the maximum stress on the undeforming bed, we find that a stable margin configuration occurs if the channel radius is lower than a critical value because the dependence of till strength on channel size is more sensitive than the dependence of the maximum stress on channel size.

For fixed material properties and far-field loading the channel radius and the locking radius are functions of the water flux in the channel alone. Figure 6 plots R and R_{lock} as a function of Q_w for the parameters in Table 1 and a Glen's law rheology. At low water fluxes the channel radius is larger than the locking radius R_{lock}, and thus the margin configuration is not stable. However, R_{lock} increases faster with Q_w than R, leading to a stable margin configuration above a critical flux water flux.

Using our formulae for R and R_{lock} we solve for the critical water flux that must be exceeded for a stable margin to occur,

$$Q_{lock} = 2^{25/17} \left(\frac{n_m}{\pi S^{1/2}}\right)^{15/17} \left(1 + \frac{2}{\pi}\right)^{10/17} \left(\frac{\chi}{2f}\right)^{96/17} \left(\frac{\pi A L \rho_{ice}}{\rho_w g S Q_w}\right)^{32/17} \left(\frac{3J_{tip}}{4\pi A}\right)^{24/17}. \quad (33)$$

Figure 7 plots Q_{lock} as a function of A for different values of f and τ_{lat}. We choose this range of A based on the scatter in the experimentally measured values of A at 0 °C reported in *Cuffey and Paterson* [2010]. We observe a strong dependence of the critical water flux on A, with the smallest values of A leading to the smallest values of Q_{lock}. If based on the estimates in *Perol et al.* [2015] we assume that a typical water flux in a channel is approximately 0.1 m^3/s then Figure 7 suggests that the locking point is not

collocated with a channel at Dragon margin if the ice deforms with a Glen's law rheology. Choosing a single value for the water flux, which varies significantly in space and time, is somewhat unsatisfying and long-term we hope to incorporate our analysis into a model for ice stream hydrology that will allows us to solve for the water flux in the channel instead of just picking a value. However, developing and analyzing such a model is far beyond the scope of this paper.

We observe a strong dependence of Q_{lock} on τ_{lat} for all three stress exponents, as shown in Figure 8. If we again choose a typical channel flux to be 0.1 m^3/s then for a Glen's law rheology the locking point can coincide with a channel if the lateral stress is less than ∼50 kPa and for dislocation creep the locking point can coincide with a channel if the lateral stress is less than ∼115 kPa. Using data for a range of shear margins from *Joughin et al.* [2002], *Perol and Rice* [2015] estimated that $\tau_{lat} \approx 100-135$ kPa. From these observations we conclude that there are some scenarios where the locking point can be collocated with a drainage channel, though this configuration is not probably typical and only occurs in regions of high water flux. Predicting specific locations where the drainage channel is likely collocated with a drainage channel is difficult due to the poor constraints on the presence of drainage channels within shear margins and the water fluxes through such a channel. Note that our results are sensitive to the assumed rheology, and collocation of the locking point with a channel can only occur if the ice deformation at the locking point follows the dislocation creep rheology of *Durham et al.* [1997], which dominates at the highest shear stresses. Our results highlight the importance of properly determining how ice deforms over a range of shear stresses, grain sizes, and temperatures.

7. Discussion

In this paper we investigated when the locking point can be collocated with a drainage channel within a shear margin. We showed that the presence of the channel limits the maximum shear stress on the undeforming bed and alters the yield strength of the till by changing the normal stress on the ice-till interface. By determining when the shear stress on the undeforming bed is always less than the till strength we found that the locking point can be collocated with a drainage channel only if the water flux in the channel exceeds a critical flux that depends sensitively on the ice rheology.

Our analysis complements *Perol et al.* [2015], which demonstrated how a drainage channel not collocated with the locking point can select the margin location by raising the yield strength of the till over a broad zone within the shear margin. In contrast, our analysis studied the scenario where the locking point is collocated with a channel and focused on understanding how the presence of a channel alters the shear stress and normal stress resolved on the undeforming bed. However, our conclusions are in good agreement with *Perol et al.* [2015]. Figure 8 shows that for the Glen's law rheology (i.e. $n = 3$) used exclusively in *Perol et al.* [2015] the locking point cannot be collocated with a channel, which is the same conclusion reached in *Perol et al.* [2015].

The two distinct hydrologic mechanisms presented in this paper and *Perol et al.* [2015] – one with the locking point collocated with the channel and the other with the locking point occurring inboard of the channel on a temperate bed – both become more effective as the flux in the channel increases. Thus, the hydrologic mechanisms are most likely to select the shear margin location in regions of high water flux. When the hydrologic mechanisms are ineffective we expect the margin location to be controlled by where the

subglacial till freezes, a scenario studied in *Jacobson and Raymond* [1998], *Schoof* [2012], and *Haseloff* [2015].

7.1. Limitations of model

In this subsection we outline the limitations of our model and discuss how these limitation may alter our conclusions. The solution from *Nye* [1953] used to model creep closure of the channel was developed for axisymmetric creep closure of a circular hole and implicitly assumes free slip boundary conditions at the bed. However, our boundary conditions are no slip on one side of the channel and a deforming bed providing a finite basal resistance on the other. *Weertman* [1972] suggested that the change to no slip boundary conditions at the bed will alter the strength of the undeforming bed in several ways. First, additional basal resistance will lower the creep closure rate, leading to a lower pore pressure in the channel and thus a stronger bed. If the realistic boundary conditions lead to a creep closure rate equal to half the value predicted by equation (26) then the effective stress in the channel increases by a factor of 2^n, which highlights the importance of accurately determining n. Second, *Weertman* [1972] showed that for a Newtonian rheology the no slip boundary condition reduces the normal stress applied to the bed, and thus the yield strength of the till, far from the channel. However, *Weertman* [1972] was unable to produce a formula for the normal stress immediately adjacent to the channel or account for a spatially variable in-plane strain rate and a nonlinear rheology. Finally, our creep closure model neglects to couple the in-plane strain rates from channel closure with the large anti-plane strain rates present at the locking point. This important coupling, first noted in *Röthlisberger* [1972] and studied further in *Weertman* [1972] and *Fernandes et al.* [2014], is expected to lead to easier channel closure, and thus a lower effective stress and

yield strength adjacent to the channel. Currently it is unclear how the three uncertainties associated with the closure model, one of which raises τ_{yield} and two of which lower τ_{yield}, balance each other to control the yield strength of the till near a drainage channel. Note that the coupling with lateral flow in our model through the nonlinear ice rheology is physically different from the dependence on lateral flow in *Suckale et al.* [2014], which highlighted that the advection of cold ice into the margin driven by lateral gradients in ice thickness greatly influences the large scale temperature structure of a shear margin. In our model we consider a channel sitting within a broad region of temperate ice, and thus temperature gradients are unimportant and we are insensitive to the effects of advection.

Determining how the presence of a channel alters the till yield strength is important for the deforming bed as well as the undeforming bed. As shown in Section 4.3, the basal resistance provided by the deforming bed near the channel plays an important role in setting the maximum stress on the undeforming bed. However, we did not explore this effect in depth because the exact functional form of the basal resistance is unclear. To clarify the spatial variations in basal resistance on the deforming bed requires new calculations accounting for realistic basal boundary conditions and the coupling between in-plane and anti-plane deformation, as discussed earlier in this section. Note that a broad zone of elevated basal resistance will lower J_{tip}, as shown in *Perol et al.* [2015], leading to a substantially lower value of Q_{lock} and a greater likelihood that the locking point could be collocated with a drainage channel.

Next we discuss our assumed channel geometry. The asymmetry of the boundary conditions across the channel will lead to asymmetric creep closure of the channel, suggesting that our assumption of a semi-circular may not be valid. If creep closure is less rapid near

the undeforming bed then the radius of curvature of the channel wall at the undeforming bed may be greater than the average channel radius, making the stress limiting effects of the channel more effective. Note that the asymmetry of the boundary conditions will lead to different normal stresses on the deforming and undeforming bed, leading to a jump in the till yield strength across the channel. Furthermore, asymmetry in the creep closure of the channel will lead to gradual migration of the channel towards the undeforming bed. The upper bound for this migration rate is the melt rate at the channel wall, which rarely exceeds 0.1 m/a in our calculations.

Another limitation of the model regards the details of how the subglacial till deforms. For simplicity we assume a deforming bed on one side of the channel and an undeforming bed on other, but do not explicitly model how this transition occurs in the till. Furthermore, we assume that the entirety of the channel is incised into the ice, ignoring the possibility that a channel may develop in the till or other physical effects that may become important at high effective stresses such as the penetration of ice into the till studied in *Rempel* [2009]. If the radius of curvature at the channel wall is lowered by incision into the till then our mechanism for limiting the maximum stress using a channel becomes less effective.

Finally our model could be extended to account for non-steady state effects such as variable water flux, time-dependent transport of water to the channel, and evolving channel shape. Non-steady state effects could be particularly important when determining how our results relate to observations of margin migration.

7.2. Importance of ice rheology

While a simple Glen's law rheology may be a good approximation for ice stream scale simulations, our paper highlights the importance of properly determining the dominant physical processes that allow ice to deform over a range of stresses. Figures 7 and 8 show that the critical water flux that controls if the transition from a deforming to an undeforming bed across a channel is stable depends sensitively on the assumed values of n and A. More generally, the closure rate of and pore pressure in a channel, important considerations in all models of subglacial drainage channels, depend strongly on A and n.

The high shear stresses present at the locking point may allow deformation to occur solely through dislocation creep. Dislocation creep is the dominant deformation mechanism ice at the highest shear stresses and is governed by $n = 4$ [*Durham et al.*, 1997]. If we assume a grain size of 4 mm – a typical grain size observed in the shear margin cores from *Jackson and Kamb* [1997] – Figure 60.3 from *Goldsby* [2006] predicts that dislocation creep dominates for stresses exceeding $\sim$ 200 kPa. Figure 4 shows that this critical stress is lower than the shear stress expected on the undeforming bed for a channel with radius 1 m, and thus $n = 4$. However, the stress concentration at the locking point could drive significant grain size reduction. If the grain size is reduced to 1 mm then dislocation creep dominates above $\sim$ 1 MPa, and if the grain size reaches 100 μm then dislocation creep dominates above $\sim$ 2 MPa. For comparison, *Perol et al.* [2015] and Figure 4 show that peak stresses within the shear margin are at least a few hundred kPa, though it should be noted that the analysis in *Perol et al.* [2015] uses a Glen's law rheology with the temperature dependence from *Cuffey and Paterson* [2010]. If dislocation creep is not the dominant deformation mechanism then the grain-boundary sliding regime governed by

$n = 1.8$ described in *Goldsby and Kohlstedt* [2001] dominates. The concentrated stresses present at the locking point may produce a fabric in the ice. If this occurs then the value of A governing the creep closure of the channel will differ from the value of A governing the shear stress resolved on the bed.

In Section 2 we assumed that the melt content of the ice immediately adjacent to the channel could be neglected when determining values of A and n. However, this assumption may not be valid for all shear margins, especially if a large quantity of melt is generated in the temperate ice. Accurately determining the effect of melt fraction on rheology is beyond the capability of current experiments, though the experiments in *Duval* [1977] and *Lliboutry and Duval* [1985] showed that a melt fraction of just 1.1% increases A by about a factor of three. Other experiments performed on partially molten olivine – which deforms through similar physical mechanisms as ice – showed increasing the melt fraction promotes grain boundary diffusion creep, which is governed by $n = 1$ [*Cooper and Kohlstedt*, 1986]. Thus, it may not be sufficient to just make A a function of the melt fraction, and there may also be a change in n at a given shear stress.

When predicting the melt content in the ice adjacent to the channel it may be helpful to consider two end-members dictated by the balance between subglacial drainage and englacial drainage. For the case where the subglacial transport of melt – either through the till or along the ice-till interface – is more efficient than englacial transport we expect melt to be routed to the bed before flowing to the channel. For this scenario we expect the water content in the temperate ice immediately adjacent to the channel to be negligible. In contrast, if subglacial flow is inefficient then melt may be routed to the channel englacially, implying a significant water content in the ice next to the channel, and thus a much

larger value of A. Our qualitative argument assuming that drainage naturally selects the most efficient route from where melt is generated to the channel is motivated by the quantitative analysis in *Fisher* [1951] that studied how diffusion along grain boundaries and diffusion through individual crystals balance to control diffusion into a polycrystalline metal. *Fisher* [1951] showed that if the grain boundary diffusivity is significantly higher than the diffusivity for an individual crystal then the most efficient way to penetrate into the polycrystal is to diffuse as far as possible along the grain boundary before leaking into the adjoining crystal. In this analogy subglacial drainage is equivalent to diffusion along a grain boundary and englacial drainage is equivalent to diffusion through an individual crystal.

8. Conclusions

Our paper investigated when the transition from a deforming to an undeforming bed can occur across a subglacial drainage channel. We showed that the presence of a channel at the locking point limits the maximum shear stress resolved on the undeforming bed and alters the till strength by changing the normal stress on the ice-till interface. Comparing stress and strength on the undeforming bed, we determined that the locking point can be collocated with a drainage channel if and only if the water flux in the channel exceeds a critical value. For a Glen's law rheology this critical flux is unrealistically large if the average lateral shear stress in the shear margin exceeds $\sim 35 - 50$ kPa. However, for the dislocation creep rheology of *Durham et al.* [1997] the critical flux is substantially lower, and the locking point can be collocated with the channel if the average lateral shear stress in the shear margin is less than $\sim 85 - 115$ kPa. From these observations we conclude

that there are some scenarios where the locking point can be collocated with a drainage channel, though this configuration is probably not typical.

Acknowledgments. This research was supported by the National Science Foundation through the Office of Polar Programs award number 1341499 (March 2014 to February 2017), and previously grant ANT-0739444 (June 2008 to May 2012) to Harvard University. Input files used for the numerical simulations are available upon request by emailing the corresponding author at jplatt@dtm.ciw.edu The authors thank Christian Schoof, Tim Creyts and Alan Rempel for fruitful discussions.

Appendix A: Derivation of near-tip solution

In this appendix we solve for the stress field and velocity near the transition from a deforming to an undeforming bed, assuming a sharp transition at $y = z = 0$. We use the hodograph plane methods from *Rice* [1967] and *Rice* [1968b] to solve for the downstream velocity profile as well as the stress field. Our approach is different from *Suckale et al.* [2014] because we need to solve for the downstream velocity profile, as well as the stress field. The downstream velocity profile is later used as a boundary condition in numerical simulations for the stress field around a channel.

To begin we define the Legendre transform of the downstream velocity u

$$\psi = y\dot{\gamma}_y + z\dot{\gamma}_z - u, \tag{A1}$$

where $\dot{\gamma}_y$ and $\dot{\gamma}_z$ are the engineering strain rates defined by

$$\dot{\gamma}_y = \frac{\partial u}{\partial y} \quad , \quad \dot{\gamma}_z = \frac{\partial u}{\partial z}. \tag{A2}$$

The effective engineering strain rate is equal to $[\dot{\gamma}_y^2 + \dot{\gamma}_z^2]^{1/2}$, and the power law rheology given in equation (3) can be written as $\dot{\gamma} = 2A\tau^n$. Differentiating equation (A1) with respect to $\dot{\gamma}_y$ and $\dot{\gamma}_z$, and noting that

$$\frac{\partial u}{\partial \dot{\gamma}_y} = \dot{\gamma}_y \frac{\partial y}{\partial \dot{\gamma}_y} + \dot{\gamma}_z \frac{\partial z}{\partial \dot{\gamma}_y} \quad , \quad \frac{\partial u}{\partial \dot{\gamma}_z} = \dot{\gamma}_y \frac{\partial y}{\partial \dot{\gamma}_z} + \dot{\gamma}_z \frac{\partial z}{\partial \dot{\gamma}_z}, \tag{A3}$$

we can relate the first derivatives of ψ to the coordinates y and z through

$$\frac{\partial \psi}{\partial \dot{\gamma}_y} = y \quad , \quad \frac{\partial \psi}{\partial \dot{\gamma}_z} = z. \tag{A4}$$

Following *Rice* [1967] we rewrite the equation for mechanical equilibrium as

$$\frac{\partial y}{\partial \tau_{xy}} + \frac{\partial z}{\partial \tau_{xz}} = 0 \tag{A5}$$

and define polar coordinates in the strain plane

$$\dot{\gamma}_y = -\dot{\gamma}\sin\phi \quad , \quad \dot{\gamma}_z = \dot{\gamma}\cos\phi. \tag{A6}$$

Note that in the hodograph plane radius from the origin is equal to the equivalent engineering strain rate $\dot{\gamma}$. As shown in *Rice* [1967], the equation for mechanical equilibrium in the hodograph plane is

$$n\frac{\partial^2\psi}{\partial\dot{\gamma}^2} + \frac{1}{\dot{\gamma}}\frac{\partial\psi}{\partial\dot{\gamma}} + \frac{1}{\dot{\gamma}^2}\frac{\partial^2\psi}{\partial\phi^2} = 0. \tag{A7}$$

Note that transforming from the physical plane to the hodograph plane has turned the nonlinear equation for u into a linear equation for ψ.

Next we map the two boundary conditions in the physical plane to the hodograph plane. We can determine where these two boundary conditions map to in the hodograph plane by noting that for the traction free condition $\dot{\gamma}_z = 0$ and $\dot{\gamma}_y < 0$, while for the no slip boundary condition $\dot{\gamma}_y = 0$ and $\dot{\gamma}_z > 0$. Thus the no-slip condition maps to the positive $\dot{\gamma}_z$-axis and the traction free condition maps to the negative $\dot{\gamma}_y$-axis.

Having located the boundary conditions in the hodograph plane we next determine the form of the boundary conditions. For the no slip condition all three terms in equation (A1) vanish, leading to

$$\psi = 0 \quad \text{on} \quad \phi = 0. \tag{A8}$$

In the physical plane the traction free boundary condition occurs on $z = 0$, and thus from equation (A4) we find $\partial\psi/\partial\dot{\gamma}_z = 0$. This is equivalent to saying that the normal derivative must vanish,

$$\frac{\partial\psi}{\partial\phi} = 0 \quad \text{on} \quad \phi = \pi/2. \tag{A9}$$

Figure 9 shows a sketch of the physical plane and hodograph highlighting the equations and boundary conditions.

We solve equation (A7) with the boundary conditions given in (A8) and (A9) using the separable solution

$$\psi = -C\dot{\gamma}^{-1/n}\sin\phi, \tag{A10}$$

where the constant $C > 0$ is an arbitrary constant that we determine later and the negative sign is required to ensure that when we map back to the physical plane our solution lies in $z > 0$. Note that equation (A10) is a much simplified case of the eigenfunction expansion given in the original solution of this problem from *Rice* [1967]. Using the solution for ψ we now determine the mapping to switch between $(\dot{\gamma}, \phi)$ and (r, θ). In the hodograph plane polar coordinates defined in equation (A6) equation (A4) becomes

$$y = -\sin\phi\frac{\partial\psi}{\partial\dot{\gamma}} - \frac{\cos\phi}{\dot{\gamma}}\frac{\partial\psi}{\partial\phi}, \tag{A11}$$

$$z = \cos\phi\frac{\partial\psi}{\partial\dot{\gamma}} - \frac{\sin\phi}{\dot{\gamma}}\frac{\partial\psi}{\partial\phi}. \tag{A12}$$

Inserting the solution given in equation (A10) we find

$$y = -C\dot{\gamma}^{-(n+1)/n}\left(\left(\frac{n+1}{n}\right)\sin^2\phi - 1\right), \tag{A13}$$

$$z = \frac{n+1}{n}C\dot{\gamma}^{-(n+1)/n}\sin\phi\cos\phi. \tag{A14}$$

Dividing z by y we arrive at an equation for θ,

$$\tan\theta = \frac{(n+1)\tan\phi}{n - \tan^2\phi}. \tag{A15}$$

Noting that equation (A15) defines a quadratic equation in $\tan\phi$ we solve to find

$$\tan\phi = -\frac{(n+1)\cot\theta}{2} + \sqrt{\frac{(n+1)^2\cot^2\theta}{4} + n}. \tag{A16}$$

To find the radius r in the physical plane we use $r^2 = y^2 + z^2$, leading to

$$r = C\dot{\gamma}^{-(n+1)/n}\sqrt{\left(\frac{1+n}{n}\right)\left(\frac{1-n}{n}\right)\sin^2\phi + 1}. \tag{A17}$$

We rearrange equation (A17) to give $\dot{\gamma}$ in terms of r,

$$\dot{\gamma}^{(n+1)/n} = \frac{C}{r}\sqrt{\left(\frac{1+n}{n}\right)\left(\frac{1-n}{n}\right)\sin^2\phi + 1}, \tag{A18}$$

where $\tan\phi$ is given by equation (A16) and we use the trigonometric identity,

$$\sin^2\phi = \frac{\tan^2\phi}{1+\tan^2\phi}. \tag{A19}$$

At this point we solve for the constant C using the J-integral, which links the far-field loading to the asymptotic solution valid near the locking point. This process is greatly simplified by comparing with the solution for the stress field around a sharp transition from *Suckale et al.* [2014]. Comparing our solution for z given in equation (A12) with equation (B2) in *Suckale et al.* [2014] allows us to relate the function F defined in *Suckale et al.* [2014] to our solution through

$$F = \frac{n+1}{2n}C\dot{\gamma}^{-(n+1)/n}. \tag{A20}$$

Using the definition of F given in equation (B4) of *Suckale et al.* [2014] we arrive at

$$C = \frac{2n(2A)^{1/n}J_{tip}}{\pi(n+1)}. \tag{A21}$$

Determining the constant C completes our solution for ψ.

Finally we invert for u using

$$u = \dot{\gamma}\frac{\partial\psi}{\partial\dot{\gamma}} - \psi, \tag{A22}$$

allowing us to find the velocity field around the locking point in terms of $\dot{\gamma}$ and ϕ,

$$u = \frac{(n+1)C}{n}\dot{\gamma}^{-1/n}\sin\phi. \tag{A23}$$

Using equations (A16) and (A18) we rewrite this in terms of r and θ to find,

$$u = \left(\frac{2A(n+1)}{n}\right)^{1/(n+1)} \left(\frac{2J_{tip}}{\pi}\right)^{n/(n+1)} r^{1/(n+1)} g(\theta), \tag{A24}$$

where the shape of the velocity field is given by the function

$$g(\theta) = \left(\frac{n^2 f^{n+1}}{(n^2+f)(1+f)^n)}\right)^{1/(2n+2)} \tag{A25}$$

and the function $f(\theta)$ is

$$f(\theta) = n + \frac{(n+1)^2}{2}\cot^2\theta - (n+1)\cot\theta\sqrt{\frac{(n+1)^2}{4}\cot^2\theta + n}. \tag{A26}$$

Noting that $\partial u/\partial y = 0$ on the undeforming bed, we inserting the derivative of u with respect to z into the power law given in equation (3) to find the stress on the undeforming bed,

$$\tau_{sharp} = \left(\frac{nJ_{tip}}{(n+1)A\pi y}\right)^{1/(n+1)}. \tag{A27}$$

Appendix B: Solution for circular channel and Newtonian rheology

Here we develop an analytic solution for the stress on the undeforming bed a semi-circular channel in ice with a Newtonian rheology. Because our solution relies on complex variables, it cannot be extended to other stress exponents $n \neq 1$. To begin we assume that the basal resistance acting on the deforming bed is much smaller than the concentrated stresses at the locking point, allowing us to model the deforming bed as a stress free boundary. After we generalize the solution to account for the finite basal resistance that *Perol et al.* [2015] argued is important to a drainage channel in the margin

B1. Negligible basal resistance

To begin we define the complex coordinate $\xi = y + iz = re^{i\theta}$ and the holomorphic function G such that

$$u = 2A\Im(G(\xi)), \tag{B1}$$

where $\Im(G)$ indicates the imaginary part of G. Differentiating G with respect to ξ we find

$$G'(\xi) = \tau_{xz} + i\tau_{xy}. \tag{B2}$$

Based on the small-scale yielding assumption validated in Section 3, we require that G match the solution for a sharp transition as $\xi \to \infty$,

$$G'(\xi) \to \left(\frac{J_{tip}}{2A\pi}\right)^{1/2} \xi^{-1/2} \quad \text{as} \quad \xi \to \infty. \tag{B3}$$

In addition we have a traction free boundary condition at the channel face $r = R$,

$$\tau_{zy}n_y + \tau_{xz}n_z = 0, \tag{B4}$$

where n_y and n_z are the y and z components of the unit normal to the channel wall respectively. Using our definition of ξ and equation (B2) we rewrite the traction free condition on the channel face as

$$\Im[e^{i\theta}G'(\xi)] = 0. \tag{B5}$$

To match the stress free boundary condition at $r = R$ we look for a series solution,

$$G'(\xi) = \left(\frac{J_{tip}}{2A\pi}\right)^{1/2} \xi^{-1/2} \left(1 + \sum_{k=1}^{\infty} \frac{C_k}{\xi^k}\right), \tag{B6}$$

using the fact that all holomorphic functions are analytic to write $G'(\xi)$ as a series expansion in ξ. Our series expansion naturally satisfies the no slip condition at $\theta = 0$ and the

traction free boundary condition at $\theta = \pi$. Inserting (B6) into (B5) leads to

$$\Im\left[e^{i\theta/2}\left(1+\sum_{k=1}^{\infty} C_k R^{-k} e^{-ik\theta}\right)\right] = 0, \tag{B7}$$

which is satisfied by setting $C_1 = R$ and $C_k = 0$ for $k > 1$. Thus, our final solution for $G'(\xi)$ is

$$G'(\xi) = \left(\frac{J_{tip}}{2A\pi}\right)^{1/2} \xi^{-1/2}\left(1+\frac{R}{\xi}\right). \tag{B8}$$

We extract the shear stress along the undeforming portion of the bed by setting $\xi = y$ to arrive at

$$\tau_{xz} = \left(\frac{J_{tip}}{2A\pi y}\right)^{1/2}\left(1+\frac{R}{y}\right). \tag{B9}$$

B2. Finite basal resistance

The method used to calculate the maximum stress on the locked portion of the bed for a Newtonian rheology and a circular channel can be generalized to allow for a non-zero basal stress. When the deforming bed applies a non-zero shear stress τ_f to the ice the far-field solution for a singular crack becomes

$$\tau_{xz} + i\tau_{xy} = \tau_f + \left(\frac{J_{tip}}{2A\pi}\right)^{1/2} \xi^{-1/2}, \tag{B10}$$

which is equal to the linear superposition of a constant stress field $(\tau_{xy}, \tau_{xz}) = (0, \tau_f)$ and the solution for a sharp transition assuming that the bed provides no resistance. To find a solution that approaches the singular solution as $\xi \to \infty$ we again use a series expansion,

$$\tau_{xz} + i\tau_{xy} = \tau_f + \left(\frac{J_{tip}}{2A\pi}\right)^{1/2} \xi^{-1/2}\left(1+\sum_{k=1}^{\infty}\frac{C_k}{\xi^k}\right). \tag{B11}$$

Inserting this expansion into the traction free boundary condition given in equation (B5) we arrive at

$$\tau_f \sin\theta + \sqrt{\frac{J_{tip}}{2\pi AR}}\sum_{k=0}^{\infty} C_k \sin((1/2-n)\,\theta)) = 0, \tag{B12}$$

where we have set $C_0 = 1$. To find the coefficients C_k we use the series expansion

$$\sin\theta = \sum_{k=1}^{\infty} D_k \sin\left((n-1/2)\theta\right) \quad , \quad -\pi \leq \theta < \pi, \tag{B13}$$

which is equivalent to

$$\sin 2\psi = \sum_{k=1,3,5,\ldots}^{\infty} D_k \sin\left(n\psi\right) \quad , \quad -\frac{\pi}{2} \leq \psi < \frac{\pi}{2}. \tag{B14}$$

To find the coefficients D_k we use the orthogonality condition

$$\int_{-\pi/2}^{\pi/2} \sin(n\psi)\sin(m\psi)\mathrm{d}\psi = \frac{\pi}{2}\delta_{mn}, \tag{B15}$$

where δ_{mn} is the Kronecker delta and m, n are both odd. Using equation (B15) we calculate the formula for D_k,

$$D_k = \frac{2}{\pi}\int_{-\pi/2}^{\pi/2} \sin(2\psi)\sin(k\psi)\mathrm{d}\psi, \tag{B16}$$

and evaluate this to find

$$D_k = \frac{8}{\pi(k^2-4)}(-1)^{\frac{(k+1)}{2}}. \tag{B17}$$

Having found the values for D_k we can convert this to the coefficients C_k. We find that

$$C_1 = 1 + \frac{8\tau_f}{3\pi}\sqrt{\frac{2\pi AR}{J_{tip}}}, \tag{B18}$$

$$C_n = \sqrt{\frac{2\pi AR}{J_{tip}}}\frac{8\tau_f}{\pi(2n+1)(2n-3)}(-1)^n \quad , \quad n \geq 2. \tag{B19}$$

These coefficients allow us to calculate the stress applied to the locked portion of the bed

$$\tau_{xz} = \tau_f + \sqrt{\frac{J_{tip}}{2\pi Ay}}\left(1 + \sum_{n=1}^{\infty} C_n \left(\frac{R}{y}\right)^n\right). \tag{B20}$$

Appendix C: Generalization of locking to radius to $n \neq 3$

Here we generalize the analysis in section 6 to stress exponents $n \neq 3$. To do this we compare the maximum stress on the bed given by equation (18),

$$\chi\left(\frac{nJ_{tip}}{(n+1)\pi AR}\right)^{1/(n+1)}. \tag{C1}$$

with the yield strength of the undeforming bed adjacent to the channel from equation (30),

$$2f\left(\frac{\rho_w g S Q_w}{\pi L \rho_{ice} A R^2}\right)^{1/n}. \tag{C2}$$

Setting the stress less than or equal to the yield strength of the undeforming lead to the inequality,

$$\chi\left(\frac{nJ_{tip}}{(n+1)\pi AR}\right)^{1/(n+1)} < 2f\left(\frac{\rho_w g S Q_w}{\pi L \rho_{ice} A R^2}\right)^{1/n}. \tag{C3}$$

We rearrange to find the critical locking radius below which a stable margin configuration occurs,

$$R < R_{lock}, \tag{C4}$$

where the locking radius is defined as

$$R_{lock} = \left(\frac{2f}{\chi}\right)^{\frac{n(n+1)}{n+2}} \left(\frac{\rho_w g S Q_w}{\pi L \rho_{ice} A}\right)^{\frac{n+1}{n+2}} \left(\frac{\pi A(n+1)}{nJ_{tip}}\right)^{\frac{n}{n+2}}. \tag{C5}$$

Recalling that for fixed material properties and loading conditions R and R_{lock} depend on the water flux Q_w alone, we rewrite the inequality (C5) as

$$Q_w > Q_{lock}, \tag{C6}$$

where the critical water flux that must be exceeded for locking to occur is

$$Q_{lock} = 2^{\frac{5(n+2)}{5n+2}} \left(\frac{n_m}{\pi S^{1/2}}\right)^{\frac{3(n+2)}{5n+2}} \left(1+\frac{2}{\pi}\right)^{\frac{2(n+2)}{5n+2}} \left(\frac{\chi}{2f}\right)^{\frac{8n(n+1)}{n+2}} \left(\frac{\pi L \rho_{ice} A}{\rho_w g S}\right)^{\frac{8(n+1)}{5n+2}} \left(\frac{nJ_{tip}}{\pi A(n+1)}\right)^{\frac{8n}{5n+2}}. \tag{C7}$$

References

Alley, R. B., D. D. Blankenship, C. R. Bentley, and S. T. Rooney (1986), Deformation of till beneath ice stream B, West Antartica, *Nature*, 322, 57-59.

Bamber, J. L., D. G. Vaughan, and I. Joughin (2000), Widespread complex flow in the interior of the Antarctic ice sheet, *Science*, 287, 1248-1250.

Barenblatt, G. I. (1959), On the equilibrium cracks formed in brittle failure, *Journal of Applied Mathematics and Mechanics*, 23(3), 893-900.

Ben Amar, M., and J. R. Rice (2002), Exacts results with the J-integral applied to free-boundary flows, *Journal of Fluid Mechanics*, 461, 321-341.

Bilby, B. A., and J. D. Eshelby (1968), Dislocations and the theory of fracture, in *Fracture, an Advanced Treatise*, vol. II, edited by H. Liebowitz, pp. 99-182, Academic, New York.

Bilby, B. A., A. H. Cottrell, and K. H. Swinden (1963), The spread of plastic yield from a notch, *Proceedings of the Royal Society A*, 272 (1350), 304314, doi:10.1098/rspa.1963.0055.

Bindschadler, R. A., and P. L. Vornberger (1990), A VHRR imagery reveals Antarctic ice dynamics, *Eos*, 71(23).

Blankenship, D. D., C. R. Bentley, S. T. Rooney, and R. B. Alley (1986), Seismic measurements reveal a porous layer beneath an active Antarctic ice stream, *Nature*, 322, 54-57.

Blankenship, D. D., C. R. Bentley, S. T. Rooney, and R. B. Alley (1987), Till beneath ice stream B 1. Properties derived from seismic travel times, *Journal of Geophysical Research*, 92, 8,903-8,911.

Catania, G. A., T. A. Scambos, H. Conway, and C. F. Raymond (2006), Sequential stagnation of Kamb Ice Stream, West Antarctica, *Geophysical Research letters*, 33, L14502.

Cherepanov, G. (1968), Cracks in solids, *International Journal of Solids and Structures*, 4 (8), 811-831.

Clarke, T. S., C. Liu, N. E. Lord, and C. R. Bentley (2000), Evidence for a recently abandoned shear margin adjacent to ice stream B2, Antarctica, from ice-penetrating radar measurements, *Journal of Geophysical Research*, 105, 13,409-13,422.

Cooper, R. F., and D. L. Kohlstedt (1986), Rheology and structure of olivine-basalt partial melts, *Journal of Geophysical research*, 91, 9315-9323.

Cuffey, K., and W. S. Paterson (2010), *The physics of glaciers (fourth edition)*, Butterworth-Heinemann.

Dugdale, D. S. (1960), Yielding of steel sheets containing slits, *Journal of the Mechanics and Physics of Solids*, 8, 100-104.

Durham, W. B., S. H. Kirby, and L. A. Stern (1997), Creep of water ices at planetary conditions: A compilation, *Journal of Geophysical Research*, 102, 16,293-16302.

Duval, P. (1977), The role of the water content on the creep rate of polycrystalline ice, in *Isotopes and impurities in Snow and Ice*, IAHS Publications, 118, 29-33.

Echelmeyer, K. A., W. D. Harrison, C. Larsen, and J. E. Mitchell (1994), The role of the margins in the dynamics of an active ice stream, *Journal of Glaciology*, 40 (136), 527-538.

Echelmeyer, K. A., and W. D. Harrison (1999), Ongoing margin migration of Ice Stream B, Antarctica, *Journal of Glaciology*, 45 (150), 361-369.

Fernandes, M. C., C. R. Meyer, and J. R. Rice (2014), Röthlisberger channel model with anti-plane shear loading superposed on in-plane compression, Abstract C33A-0357 presented at 2014 Fall Meeting, AGU, San Francisco, Calif., 15-19 Dec.

Fisher, J. C. (1951), Calculation of diffusion penetration curves for surface and grain boundary diffusion, *Journal of Applied Physics*, 22 (1), 74-77.

Goldman, N. L., and J. W. Hutchinson (1975), Fully plastic crack problems: The center-cracked strip under plane strain, *International Journal of Solids and Structures*, 11 (5), 575-591.

Goldsby, D. L., and D. L. Kohlstedt (2001), Superplastic deformation of ice: Experimental observations, *Journal of Geophysical research*, 106, 11,017-11,030.

Goldsby, D. L. (2006), Superplastic flow of ice relevant to glacier and ice-sheet mechanics, in *Glacier Science and Environmental Change*, edited by P. G. Knight, Blackwell Publishing.

Harrison, W. D., K. A. Echelmeyer, and C. Larsen (1998), Measurements of temperature in a margin of Ice Stream B, Antarctica: implications for margin migration and lateral drag, *Journal of Glaciology*, 44 (148), 615-624.

Haseloff, M. (2015), Modelling the migration of ice stream margins, *PhD thesis*, The University of British Columbia, Canada.

Iverson, N. R., T. S. Hooyer, and R. W. Baker (1998), Ring-shear studies of till deformation: Coulomb-plastic behavior and distributed strain in glacier beds, *Journal of Glaciology*, 44 (148), 634-642.

Jackson, M., and B. Kamb (1997), The marginal shear stress of Ice Stream B, West Antarctica, *Journal of Glaciology*, 43 (145), 415-426.

Jacobson, H. P., and C. F. Raymond (1998), Thermal effects on the location of ice stream margins, *Journal of Geophysical research*, 103, 12,111-12,122.

Joughin, I., S. Tulaczyk, R. Bindschadler, and S. F. Price (2002), Changes in west Antarctic ice stream velocities: Observation and analysis, *Journal of Geophysical research*, 107 (B11), 2289, doi:10.1029/2001JB001029.

Kamb, B. (1991), Rheological nonlinearity and flow instability in the deforming bed mechanism of ice stream motion, *Journal of Geophysical Research*, 96, 16,585-16,595.

Kamb, B. (2001), Basal zone of the West Antarctic ice streams and its role in lubrication of their rapid motion, *Antarctic Research Series*, 77, 157-199.

Kubo, S., K. Ohji, and K. Ogura (1979), Analysis of creep crack-propagation on the basis of the plastic singular stress-field, *Engineering Fracture Mechanics*, 11 (2), 315-329.

Kyrke-Smith, T. M., R. F. Katz, and A. C. Fowler (2014), Subglacial hydrology and the formation of ice streams, *Proceedings of the Royal Society A*, 470: 20130494.

Kyrke-Smith, T. M., R. F. Katz, and A. C. Fowler (2015), Subglacial hydrology as a control on emergence, scale, and spacing of ice streams, *Journal of Geophysical Research*, 120, 1501-1514.

Landes, J. D., and J. A. Begley (1976), A fracture mechanics approach to creep crack growth, in *Mechanics of Crack Growth*, edited by J. R. Rice and P. C. Paris, pp. 128-148, Amer. Soc. for Testing and Materials (ASTM), Special Technical Publication (STP) 590, Philadelphia.

Lliboutry, L. A., and P. Duval (1985), Various isotropic and anisotropic ices found in glaciers and polar ice caps and their corresponding rheologies, *Annales Geophysicae*, 3, 207-224.

McMeeking, R. M., and R. E. Johnson (1986), On the mechanics of surging glaciers, *Journal of Glaciology*, 32 (110), 120-132.

Nye, J. F. (1953), The flow law of ice from measurements in glacier tunnels, laboratory experiments and the Jungfraufirn borehole experiment, *Proceedings of the Royal Society A*, 219, 477-489.

Perol, T., and J. R. Rice (2011), Control of the width of West Antarctic ice streams by internal melting in the ice sheet near the margins, Abstract C11B-0677 presented at 2011 Fall Meeting, AGU, San Francisco, Calif., 5-9 Dec.

Perol, T., and J. R. Rice (2015), Shear heating and weakening of the margins of West Antarctic ice streams, *Geophysical Research Letters*, doi:10.1002/2015GL063638.

Perol, T., J. R. Rice, J. D. Platt, and J. Suckale (2015), Subglacial hydrology and ice stream margin locations, *Journal of Geophysical Research*, 120, doi:10.1002/2015JF003542.

Raymond, C. F. (1996), Shear margins in glaciers and ice sheets, *Journal of Glaciology*, 42 (140), 90-102.

Raymond, C. F., K. A. Echelmeyer, I. M. Whillans, and C. S. M. Doake (2001), Ice stream shear margins, *Antarctic Research Series*, 77, 137-155.

Rempel, A. W. (2009), Effective stress profiles and seepage flows beneath glaciers and ice sheets, *Journal of Glaciology*, 55 (191), 431-443.

Rice, J. R. (1967), Stresses due to a sharp notch in a work-hardening elastic-plastic material loaded by longitudinal shear, *Journal of Applied Mechanics*, 34, 287-298.

Rice, J. R. (1968a), A path independent integral and the approximate analysis of strain concentration by notches and cracks, *Journal of Applied Mechanics*, 35, 379-386.

Rice, J. R. (1968b), Mathematical analysis in the mechanics of fracture, in *Fracture, an Advanced Treatise*, vol. II, edited by H. Liebowitz, pp. 191-311, Academic, New York.

Röthlisberger, H. (1972), Water pressure in intra- and subglacial channels, *Journal of Glaciology*, 11 (62), 177-203.

Scambos, T. A., K. A. Echelmeyer, M. A. Fahnestock, and R. A. Bindschadler (1994), Development of enhanced ice flow at the southern margin of Ice Stream D, Antarctica, *Annals of Glaciology*, 20, 313-318.

Schoof, C. (2004), On the mechanics of ice-stream shear margins, *Journal of Glaciology*, 50, 169, 208-218.

Schoof, C. (2010), Ice-sheet acceleration driven by melt supply variability, *Nature*, 468, 803-806.

Schoof, C. (2012), Thermally driven migration of ice-stream shear margins, *Journal of Fluid Mechanics*, 712, 552-578.

Schulson, E. M., and P. Duval (2009), Creep and fracture of ice, *Cambridge University Press*.

Shabtaie, S., and C. R. Bentley (1987), West Antarctic ice streams draining into the Ross ice shelf: Configuration and mass balance, *Journal of Geophysical research*, 92, 1311-1336.

Shabtaie, S., and C. R. Bentley (1988), Ice-thickness map of the West Antarctic ice streams by radar sounding, *Annals of Glaciology*, 11, 126-136.

Shreve, R. L. (1972), Movement of water in glaciers, *Journal of Glaciology*, 11 (62), 205-214.

Suckale J., J. D. Platt, T. Perol, and J. R. Rice (2014), Deformation-induced melting in the margins of the West Antarctic ice streams, *Journal of Geophysical research*, 119, 1004-1025.

Tulaczyk, S., W. B. Kamb, and H. F. Engelhardt (2000), Basal mechanics of Ice Stream B, West Antarctica 1. Till mechanics, *Journal of Geophysical research*, 105, 463-481.

van der Veen, C. J., and I. M. Whillans (1996), Model experiments on the evolution and stability of ice streams, *Annals of Glaciology*, 23, 129-137.

Weertman, J. (1972), General theory of water flow at the base of a glacier or ice sheet, *Reviews of Geophysics and Space Physics*, 10, 287-333.

Table 1. A table showing the parameters used in this paper. The values of ice thickness, ice stream width, and slope are intended to model ice stream B2 [*Joughin et al.*, 2002]. As shown in the text, these parameters cannot be varied independently, and variations in these parameters only alter the stress around the locking point through J_{tip}.

Parameter	Units	Value
Ice stream width, W	km	34
Ice sheet thickness, H	km	1
Ice sheet slope, S	–	0.0012
Basal shear stress beneath ice stream, τ_{base}	kPa	3.5
Gravitational acceleration, g	m s^{-2}	9.81
Density of ice, ρ_{ice}	kg m^{-3}	917
Density of water, ρ_w	kg m^{-3}	1000
Latent heat per unit mass, L	kJ/kg	335
Friction coefficient, f	–	0.6
Gauckler-Manning coefficient, n_m	s m$^{-1/3}$	0.01

Table 2. A table showing the parameters for the three different power law rheologies used in this paper. The rheology with $n = 3$ is Glen's law and we use the recommended value of A at 0 °C from *Cuffey and Paterson* [2010]. The $n = 4$ rheology is based upon the dislocation creep experiments rheology proposed in *Durham et al.* [1997] and is expected to dominate at the highest stresses.

Pre-factor, A	Stress exponent, n
2.4×10^{-14}, $\mathrm{Pa}^{-1}\ \mathrm{s}^{-1}$	1
2.4×10^{-24}, $\mathrm{Pa}^{-3}\ \mathrm{s}^{-1}$	3
2.2×10^{-30}, $\mathrm{Pa}^{-4}\ \mathrm{s}^{-1}$	4

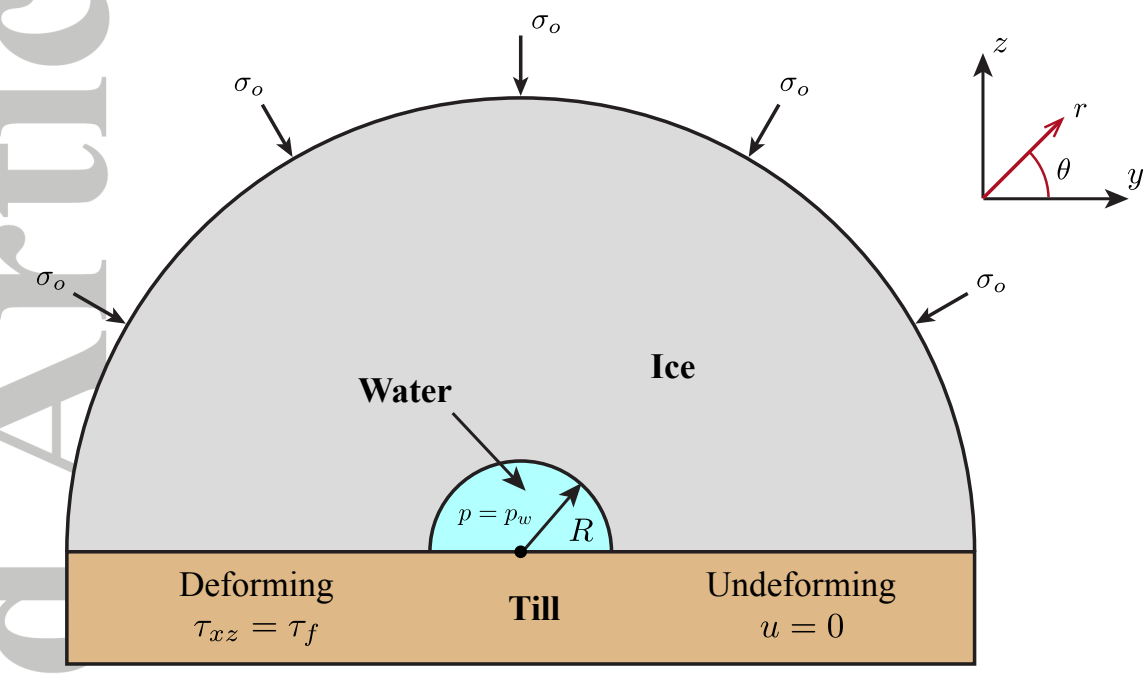

Figure 1. A sketch of the geometry used in our calculations for the deformation around the channel. We assume a semi-circular channel with a radius R incised into the ice, which rests upon a subglacial till layer. The anti-plane strain rates are calculated assuming that the bed is deforming to the left of the channel, and undeforming to the right of the channel. We model the creep closure of the channel using the pressure difference between the channel operating at a pressure p and the ice overburden σ_o.

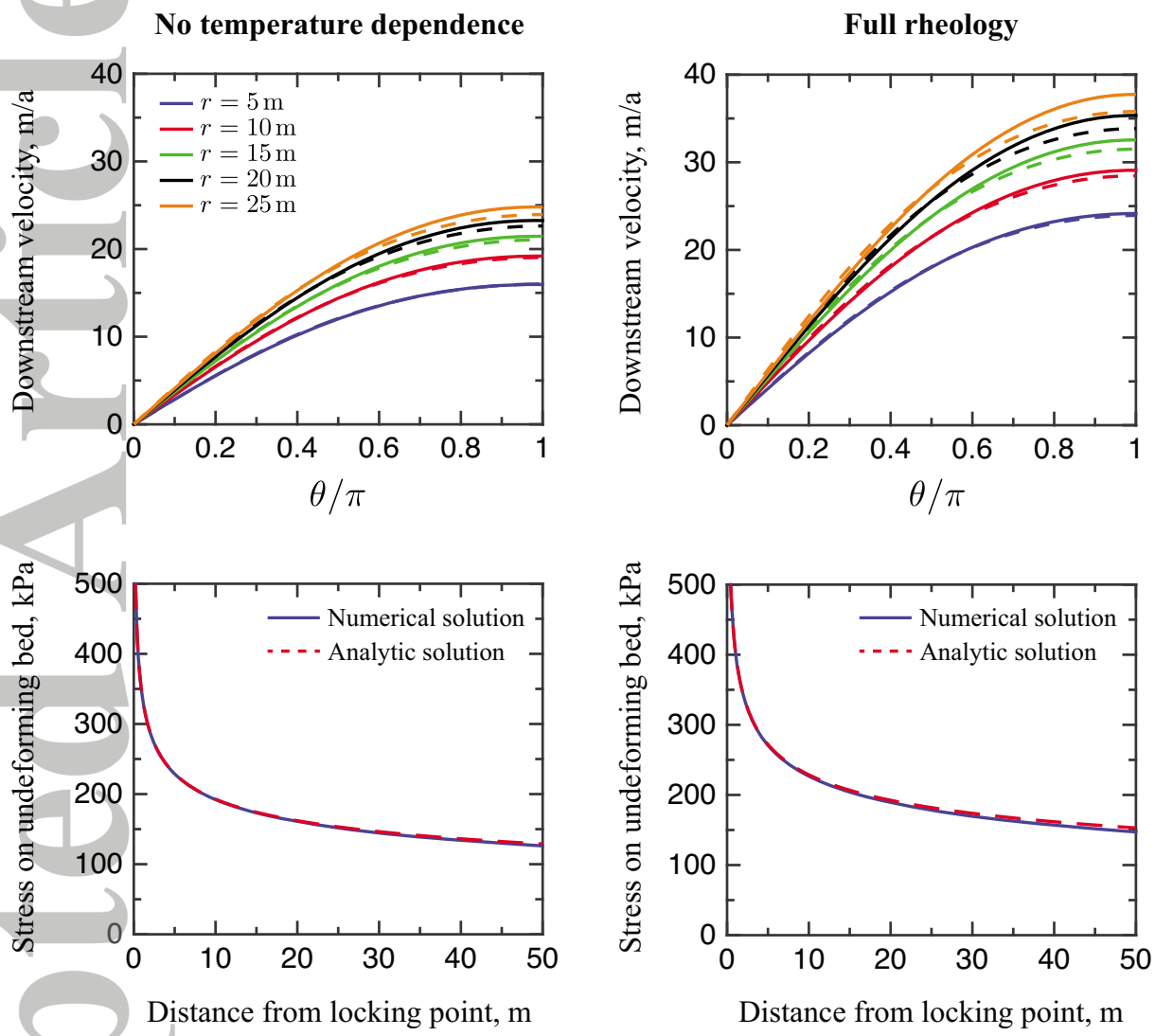

Figure 2. A plot comparing the analytic solution given in equation (A24) valid right at the locking point and numerical simulations generated using the finite element package COMSOL for the whole ice stream model from *Perol et al.* [2015]. The left hand column shows simulations that assume a constant viscosity and the right hand column shows simulations that couple deformation and temperature through a temperature dependent rheology as described in *Perol et al.* [2015]. The upper panels show the downstream velocity as a function of θ for a range of r and the lower panels shows the stress concentrated on the undeforming bed. The curve at $r = 5$ m is used to infer a best-fitting value of J_{tip} that is then used to fit all remaining curves. We see good agreement between the analytic and numerical solutions for several tens of meters, allowing us to make a small-scale yielding approximation.

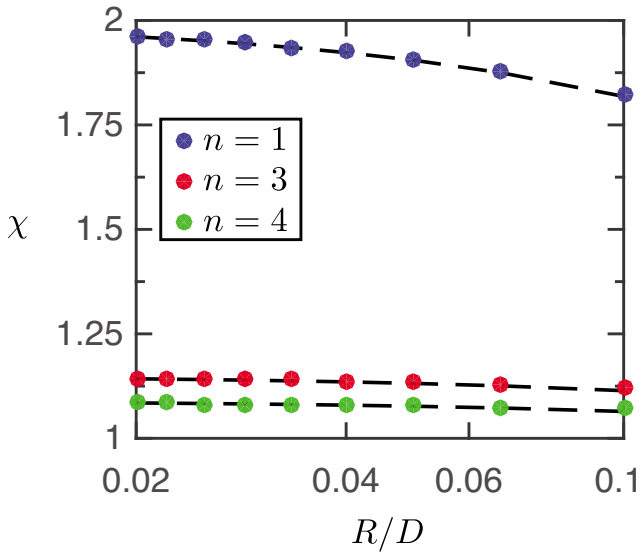

Figure 3. A plot of χ against R/D for $n = 1$, $n = 3$, and $n = 4$, alongside the fitting function $\chi = \chi_{inf}(1+R/D)^{-1/n}$. This plot allows us to infer values of χ_{inf} that are then used to determine the maximum stress resolved on the undeforming bed. We find best fitting values of χ_{inf} to be 2 for $n = 1$, 1.15 for $n = 3$, and 1.09 for $n = 4$.

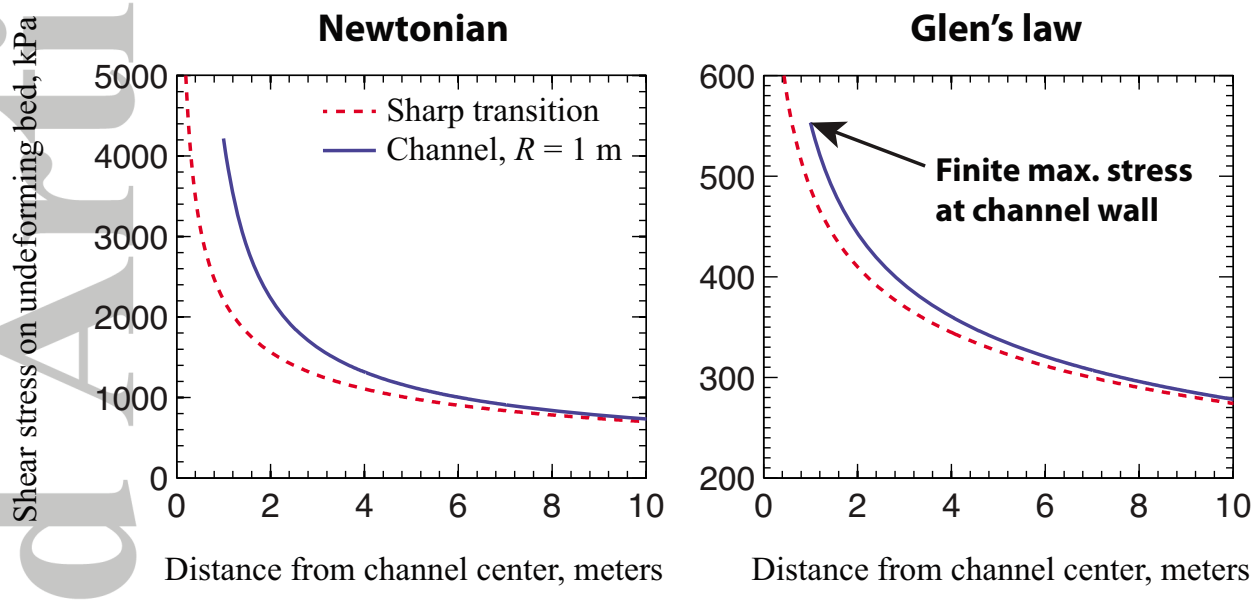

Figure 4. A plot showing the maximum stress on the undeforming bed accounting for the channel in blue alongside the prediction using the solution for a sharp margin given in equation (4) for $n = 1$ and $n = 3$. We see that the Newtonian rheology leads to significantly higher shear stresses on the bed than the Glen's law rheology, and that the solution for a sharp margin provides a reasonable approximation to the stress field accounting for the channel for all y.

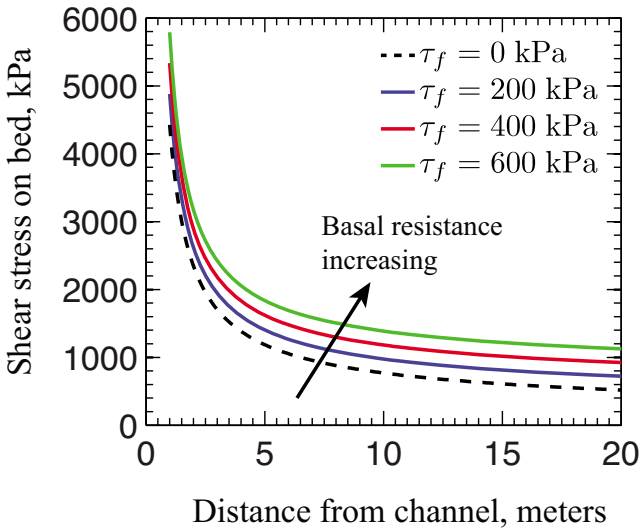

Figure 5. A plot showing how the stress on the undeforming bed varies with the basal resistance of the deforming bed τ_f for the parameters in Table 1 and $n = 1$. Our results show that for these parameter choices the dependence of maximum stress on τ_f is not significant. However, as discussed in Section 4.3, we expect the role of τ_f to become more important as τ_f becomes comparable to $\tau_{sharp}(R)$.

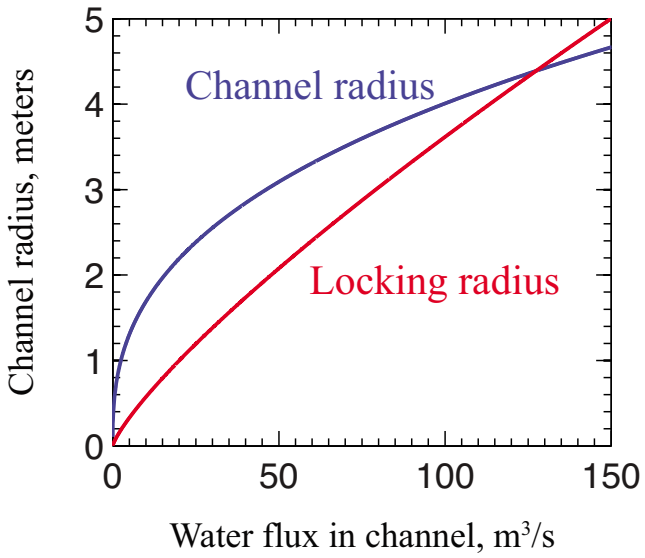

Figure 6. A plot of the channel radius R and locking radius R_{lock} against the water flux in the channel for the parameters in Tables 1 and 2 assuming a Glen's law rheology. We see that $R < R_{lock}$ – and thus a stable margin configuration exists – whenever the water flux exceeds a critical value of ~ 127 m^3/s. This water flux corresponds to a channel with a radius of 4 m.

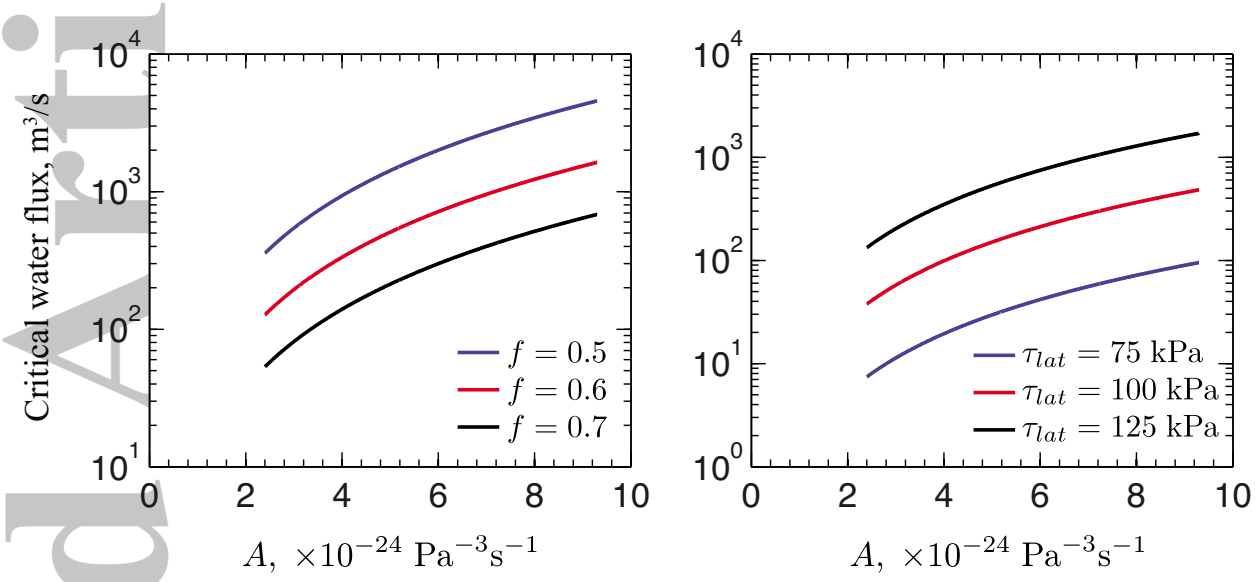

Figure 7. A plot showing how the critical water flux Q_{lock} varies for a Glen's law rheology across the range of values for A at 0 °C outlined in *Cuffey and Paterson* [2010] for different values of f and τ_{lat}. These plots were produced using the parameters in Tables 1 and 2. We see significant variability with A with higher values of A leading to larger critical fluxes. This sensitive dependence on the poorly constrained A makes it hard to predict values of Q_{lock}.

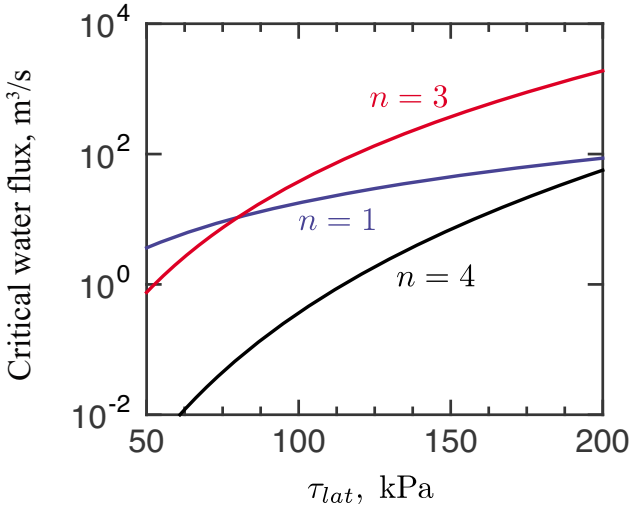

Figure 8. A plot of the critical water flux Q_{lock} against the average stress supported at the shear margin τ_{lat} for $n = 1$, $n = 3$, and $n = 4$. This plot was produced using the parameters in Tables 1 and 2. We see that Q_{lock} increases rapidly with τ_{lat}. Note that the $n = 4$ curve predicts much lower critical water fluxes that $n = 1$ and $n = 3$.

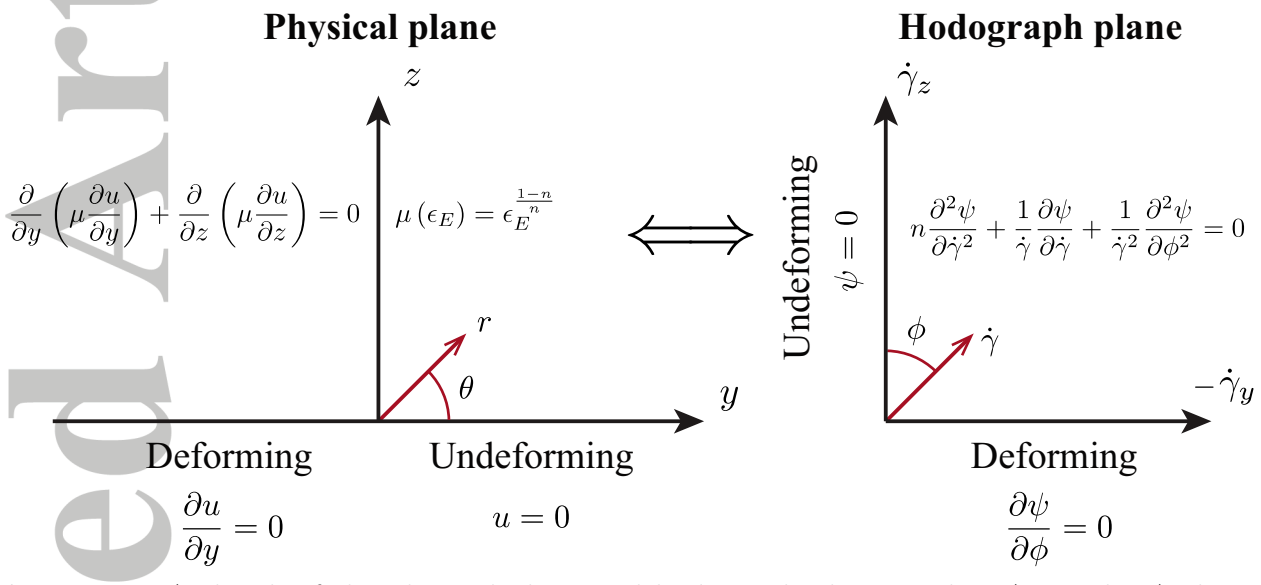

Figure 9. A sketch of the physical plane and hodograph plane used in Appendix A showing the equations solved, boundary conditions used, and coordinates in both planes.